Distribution of Decane within the Unit Cell of the Inverted Hexagonal (H_{II}) Phase of Lipid-Water-Decane Systems Determined by Neutron Diffraction†

David C. Turner,‡,§ Sol M. Gruner,*,§ and John S. Huang∥

Department of Physics, Joseph Henry Laboratories, Princeton University, Princeton, New Jersey 08544, and Exxon Research and Engineering Company, Route 22 East, Annandale, New Jersey 08801

Received May 1, 1991; Revised Manuscript Received October 28, 1991

ABSTRACT: The addition of a free alkane such as decane to lipid-water systems is known to promote the formation of a low-temperature inverted hexagonal (H_{II}) phase [Kirk, G. L., & Gruner, S. M. (1985) *J. Phys. (Paris) 46*, 761]. Kirk et al. [Kirk, G. L., Gruner, S. M., & Stein, D. E. (1984) *Biochemistry 23*, 1093] have discussed the hydrocarbon packing anisotropy in the H_{II} unit cell and have suggested that free alkane will distribute in a way that reduces this packing anisotropy by allowing the lipid chain environment to become more uniform. By combining neutron and X-ray diffraction data to do a Fourier reconstruction of the H_{II} phase of dioleoylphosphatidylethanolamine (DOPE) + water + deuterated decane, it was found that the decane preferentially partitions into the interstitial regions of the H_{II} unit cell where it should be the most effective in alleviating the hydrocarbon chain packing stress, supporting the suggestion of Kirk et al. Using the distribution of decane within the unit cell, we have calculated the lipid length distribution for the situations with and without added alkane. With a suitable molecular model, this lipid length distribution may eventually be used to calculate the free energy change upon the addition of alkane. Such a measurement is important for a more realistic understanding of the interactions which lead to the formation of the H_{II} phase.

Biomembranes contain large fractions of lipid species which promote the formation of nonlamellar phases, such as the inverse hexagonal (H_{II}) phase (Cullis et al., 1985). Since much biomembrane function depends on the existence of a stable bilayer at least most of the time, it is important to understand the effect of nonlamellar-promoting agents in a lipid mixture and the molecular forces which control the phase balance between bilayer and nonlamellar phases. It has been shown that hydrophobes such as dodecane or polyisoprenes are highly effective in promoting the formation of H_{II} phases for lipid mixtures which would otherwise be stable in bilayer form (Kirk & Gruner, 1985; Gruner, 1985; Sjölund et al., 1987; Siegel et al., 1989), especially if the lipids are electrically neutral zwitterions with a large fraction of nonlamellar promoting species. Kirk and Gruner (1985) hypothesized that this occurred because the hydrophobe preferentially partitions into the interstitial space between the H_{II} cylinders, i.e., the corners of the Wigner-Seitz cell hexagon. This hypothesis has been supported by NMR measurements (Sjölund et al., 1987; 1989; Siegel et al., 1989) but has not been directly confirmed by diffraction methods. This paper is a report of the use of X-ray and neutron diffraction to confirm the preferential partitioning of a deuterated alkane.

The greatly different neutron scattering lengths of hydrogen and deuterium [see, for instance, Knott and Schoenborn (1986)] allow a large contrast variation between protonated and deuterated regions of a specimen. The replacement of protons by deuterons has been used successfully in a number of neutron diffraction studies of lamellar lipid systems (Worcester & Franks, 1976; Büldt et al., 1979; White et al., 1981; Jacobs & White, 1989; Weiner et al., 1989); however, neutron diffraction has not been used to perform a structural analysis of lipid H_{II} phases. The neutron diffraction peaks from lipid H_{II} phases are broadened considerably by the large wavelength spread of the beam so that, typically, only a few of the diffracted orders are resolved, making it difficult to unambiguously determine their phases and to solve the structure.

The previous paper in this issue (Turner & Gruner, 1992) reports on an X-ray diffraction determination of the H_{II} phase structure. This information can be used to assist in determining the phases of the neutron diffraction peaks, and thus, the structure is a composite of information derived from both neutron and X-ray data. By comparing neutron diffraction from samples of H_{II} phase dioleoylphosphatidylethanolamine (DOPE)[1] in the presence of either protonated or deuterated decane, we have localized the distribution of deuterated decane, within the H_{II} lattice. Although this localization is limited by the resolution of the neutron diffraction, it clearly demonstrates that the decane distribution is asymmetrically distributed around the cylinder axis with a preference for the interstitial regions, thereby confirming the Kirk and Gruner (1985) hypothesis.

Much of the data presented in this paper appeared in the Ph.D. thesis of D. C. Turner (1990).

Materials and Methods

Sample Preparation. Dioleoylphosphatidylethanolamine (DOPE) was purchased from Avanti Polar Lipids (Birming-

† D.C.T. was partially supported by a Garden State Graduate fellowship and an NIH cell biology training grant. Lipid research at Princeton University is supported by grants from the DOE (DE-FG02-87ER60522), the NIH (GM32614), and the ONR (N00014-90-J-1702).

* To whom correspondence should be addressed.

‡ Current address: Naval Research Laboratories, Code 6090, Washington, D.C. 20375.

§ Princeton University.

∥ Exxon Research and Engineering Co.

[1] Abbreviations: DOPE, dioleoylphosphatidylethanolamine; POPE, 1-palmitoyl-2-oleoylphosphatidylethanolamine; L_α, lamellar liquid phase; H_{II}, inverted hexagonal phase; T_{bh}, L_α to H_{II} transition temperature.

0006-2960/92/0431-1356$03.00/0

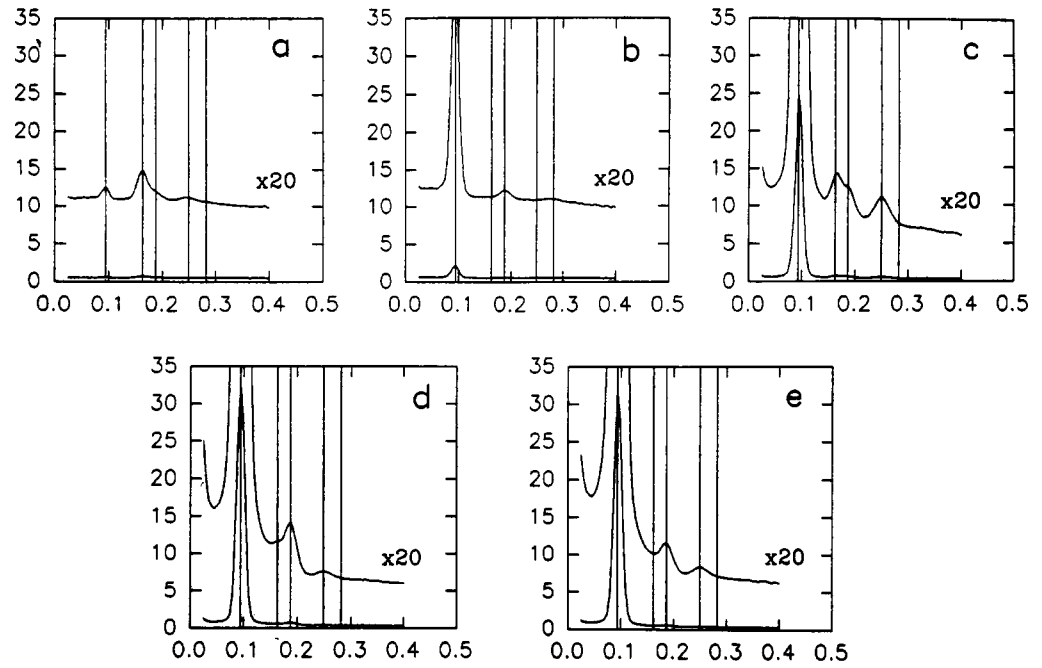

FIGURE 1: Axially integrated neutron diffraction patterns at 10 °C for (a) DOPE + H_2O, (b) DOPE + H_2O + $C_{10}D_{22}$, (c) DOPE + D_2O + $C_{10}D_{22}$, (d) DOPE + D_2O, and (e) DOPE + D_2O + $C_{10}H_{22}$. All plots are to the same scale. The vertical tic marks indicate the expected peak positions for the first five peaks (1, $\sqrt{3}$, 2, $\sqrt{7}$, 3) of a hexagonal lattice with d = 78 Å.

ham, AL), *n*-decane was purchased from Eastman Kodak (Rochester, NY). Perdeuterated *n*-decane and heavy water (D_2O) were purchased from Cambridge Isotope Labs (Woburn, MA). The following series of samples was produced: DOPE + H_2O, DOPE + D_2O, DOPE + D_2O + $C_{10}H_{22}$, DOPE + H_2O + $C_{10}D_{22}$, and DOPE + D_2O + $C_{10}D_{22}$. The samples were prepared by mixing DOPE with the appropriate alkane gravimetrically in a 10-mm culture tube to a final fraction of 35 mol % decane. The lipid + alkane was mixed with a spatula while either water or D_2O was added, until the water concentration was above excess (>60% water). This mixture, which was of a pasty texture, was allowed to equilibrate at 4 °C overnight. It was then scooped into a syringe and extruded into quartz specimen cells (1-cm diameter, 1-mm path length; NSG precision cells, 560 South Broadway, Hicksville, NY 11801) and sealed with teflon stoppers.

Diffraction Data. The diffraction data were collected at the High Flux Beam Research reactor (HFBR) at Brookhaven National Laboratory on beamline H9-B. The wavelength of the neutron beam was 4.38 Å, corresponding to an energy of 4.3×10^{-3} eV with a wavelength spread of 6–15% full width at half-maximum. The entrance pinhole at the sample was approximately 5 mm in diameter, resulting in a flux of 5×10^5 neutrons s^{-1} at the sample. Diffraction patterns were measured at 10, 25, and 50 °C for all of the samples listed above and were integrated until 130 000 counts were recorded by the detector. The diffracted neutrons were imaged using a two-dimensional ^3He wire counter which had been previously corrected for spatial uniformity. The resulting two-dimensional powder diffraction patterns were radially integrated over the full 2π radians, and the resulting one-dimensional radial intensity profiles were stored on a floppy disk (Figure 1). The peak intensities were determined by fitting a set of Gaussians plus a quadratic background to the diffraction patterns. Only the first four peaks [out to (h,k) = (2,1)] are observable because of the broad peak widths caused by the wavelength spread in the beam. The measurement error in the intensity of the strong diffraction peaks is estimated at 10%, while the error for the weak lines may be 50–100%. The intensities were then corrected for the Lorentz sin θ term [see Turner and Gruner (1992), preceding paper in this issue] and were normalized arbitrarily to the (1,0) peak at 25 °C. To account for multiplicity, the (2,1) peak intensity was divided by 2. The peak amplitudes were then evaluated by taking the square root of the corrected intensities. Table I shows the corrected amplitudes and the basis vector length or *d*-spacing (d) for the data at 10, 25, and 50 °C. Due to large peak widths, the *d*-spacings could only be measured to ±1.5 Å. To this resolution, the *d*-spacing does not change when decane is added, indicating that the radius of the water core, R_w, is probably

Table I: Neutron Diffraction Peak Amplitudes and *d*-Spacings as a Function of Temperature

	temp (°C)/*d*-spacing (Å)		
	10/78.0	25/74.5	50/70.0
	DOPE + H_2O		
(1,0)	0.96	1.00	0.49
(1,1)	2.50	3.15	2.18
(2,0)	1.41	2.11	1.28
(2,1)	0.96	1.08	0.61
	DOPE + D_2O		
(1,0)	20.68	20.45	19.12
(1,1)	1.15	0.00	0.57
(2,0)	3.04	2.65	2.19
(2,1)	1.16	0.99	0.99
	DOPE + H_2O + $C_{10}D_{22}$		
(1,0)	4.54	3.97	3.39
(1,1)	0.00	0.00	0.20
(2,0)	1.44	1.44	1.28
(2,1)	0.00	0.00	0.00
	DOPE + D_2O + $C_{10}H_{22}$		
(1,0)	20.99	20.32	18.77
(1,1)	0.00	0.00	0.00
(2,0)	2.21	1.95	1.36
(2,1)	1.36	1.32	1.21
	DOPE + D_2O + $C_{10}D_{22}$		
(1,0)	17.64	16.6	14.87
(1,1)	2.46	2.35	2.22
(2,0)	2.31	2.05	1.31
(2,1)	2.33	2.09	1.78

reduced upon the addition of decane.

Results

Reconstruction. The scattering density in the unit cell of the H_{II} phase can be determined by a Fourier cosine series:

$$\rho_s(x,y) = \frac{F(0)}{A} + \frac{1}{4A}\sum_{(i,j)\neq(0,0)} F_{ij} \cos(q_{ij_x}x) \cos(q_{ij_y}y) \quad (1)$$

where $\mathbf{r} = (x,y)$, A is the area of the unit cell, F_{ij} is the amplitude for the peak at position q_{ij}, and i,j run over all of the positive integers {1, 2, 3, ...}. The magnitudes of the peak amplitudes are determined from the square root of the diffracted intensities; however, the complex phases of the amplitudes cannot be determined directly from the intensity data. The main task that we face in doing a Fourier reconstruction is determining these phases. Fortunately, the job is simplified somewhat because the unit cell is centro- and mirror-symmetric, so the phase factors must either be + or − [see Warren (1969) for a description].

The peak amplitudes were phased by picking the phase set that gives a reconstruction most consistent with X-ray reconstructions given in the preceding paper in this issue (Turner & Gruner, 1992) and the known neutron scattering densities. This is easily accomplished by reconciling the known distribution of matter in the unit cell, which is obtained from the X-ray reconstruction, with the expected neutron scattering density for that matter distribution. Since, in all cases, the number of observed neutron peaks is four or less, the number of possible different phasing is only eight. One simply picks the phasing which yields a scattering density distribution (and thus a matter distribution) in closest agreement with the matter distribution obtained from X-ray. In addition, models of the unit cell were constructed to confirm the phase choices. X-ray diffraction models, described in accompanying the X-ray paper (Turner & Gruner, 1992), were adapted by replacing X-ray scattering lengths with neutron scattering lengths. The following scattering length densities were used: -0.55×10^{-14} cm/Å^3 for H_2O, 6.36×10^{-14} cm/Å^3 for D_2O, 1.8×10^{-14} cm/Å^3 for the phospholipid head group, -0.34×10^{-14} cm/Å^3 for the hydrocarbon chain region, and -0.85×10^{-14} cm/Å^3 for terminal methyl groups (Knott & Schoenborn, 1986; Cabane, 1986). A Debye–Waller disorder factor was necessary to properly match the observed diffraction. This factor modifies the diffracted amplitude by multiplying it by $e^{-B\sin^2(\theta)/\lambda^2}$, where $\lambda = 4.38$ Å is the wavelength of the beam, θ is the Bragg angle, and B is the Debye–Waller factor, set equal to 300 Å^2. Because the diffraction was limited to four orders, the resolution of the reconstruction was only $\Delta r \approx 30$ Å, where Δr is the full width of the resolution function which must be convoluted with the true scattering density to describe a series reconstruction limited to a few terms [see Turner and Gruner (1992) and also Turner (1990)]. It should be noted, however, that regions of high scattering contrast, such as deuterons floating in hydrocarbon, can be localized to much better than this canonical resolution [see Turner and Gruner (1992)]. This low resolution is acutally an advantage for the modeling because we could concentrate on the gross distribution of matter in the unit cell. The Fourier transform of the model scattering distribution gives the expected diffraction, which was compared to the diffraction that was observed. We define a goodness of fit parameter

$$R = \frac{\sum_{i,j}(|F_{ij}^{\text{model}}| - |F_{ij}^{\text{meas}}|)^2}{\sum_{i,j}(|F_{ij}^{\text{meas}}|)^2} \quad (2)$$

where $F_{i,j}$ are the i,jth modeled or measured peak amplitudes.

Table II: Comparison of Modeled Neutron Amplitudes with Measured Amplitudes at 25 °C for DOPE[a]

order	model $F(q)$	measured $\lvert F(q)\rvert$
	DOPE + H_2O at 25 °C, d = 74.5 Å	
(1,0)	1.00	1.00
(1,1)	−2.47	3.15
(2,0)	−2.02	2.11
(2,1)	−0.61	1.08
(3,0)	0.02	0.00
	$R = 4.1 \times 10^{-2}$	
	DOPE + D_2O at 25 °C, d = 74.5 Å	
(1,0)	20.36	20.45
(1,1)	−0.23	0.00
(2,0)	−1.72	2.65
(2,1)	−1.18	0.99
(3,0)	−1.10	0.00
	$R = 5 \times 10^{-3}$	0.00

[a] R is a measure of the quality of the fit and is described in the text.

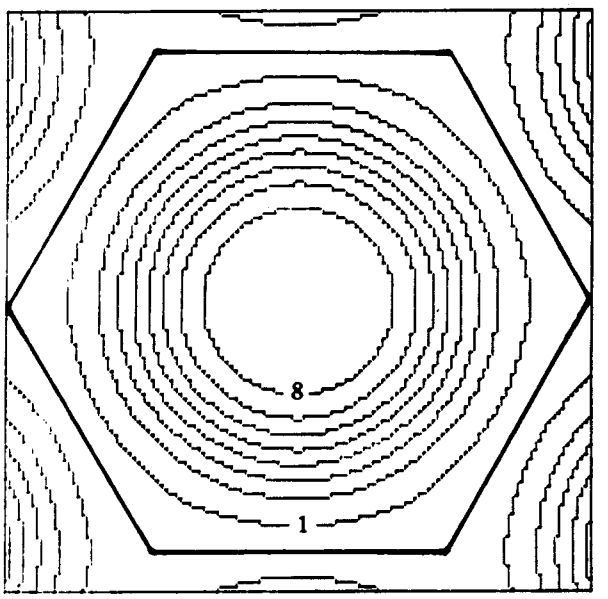

FIGURE 2: Eight-level contour plot of the four-peak reconstruction of neutron diffraction data of DOPE + D_2O at 10 °C, d = 78 Å. Contours go from lowest scattering density for contour 1 to highest scattering density for contour 8. The Wigner–Seitz cell has been drawn in bold to guide the eye. Notice that the region of highest scattering density is the water core region which contains the strongly scattering D_2O.

The best fit circular model to the DOPE + H_2O diffraction data has $R = 4.1 \times 10^{-2}$, while the best fit to DOPE + D_2O has $R = 5 \times 10^{-3}$. Table II shows both of the fits. The phasing for both data sets is +,−,−,− for the first four peaks, in agreement with the phasing found from the reconstruction most consistent with the known structure.

Figure 2 shows a four-peak Fourier reconstruction of DOPE + D_2O at 10 °C using the phasing +,−,−,−. The unit cell size is 78 Å, and the resolution of the reconstruction is $\Delta \approx 30$ Å. At this resolution the reconstruction does not change appreciably when normal decane is added (not shown). Both show an excess of scattering density in the water core, due to the D_2O, gradually decreasing to the low scattering density of the hydrocarbon region. The low resolution precludes the measurement of subtle differences between these samples, such as a small change in water core radius. Other interesting effects that could possibly be measured with higher resolution are water penetration into the lipid region and differences in effect between deuterated and protonated isomers of water and alkane. With these data, we will concentrate on the gross

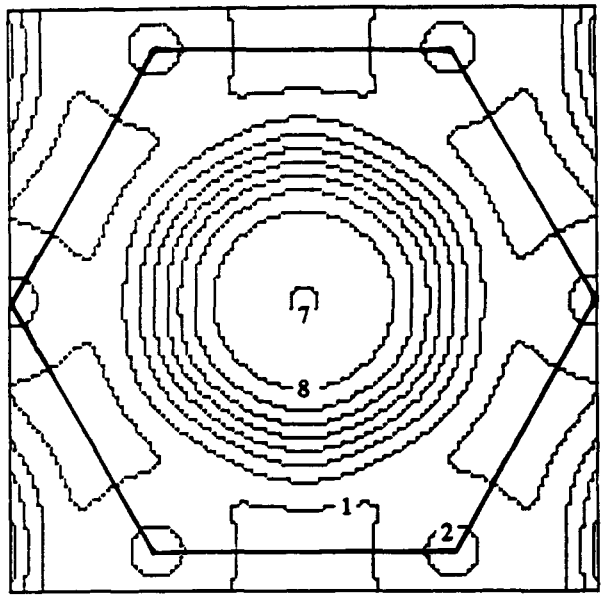

FIGURE 3: Four-peak reconstruction of neutron diffraction data for DOPE + D_2O + $C_{10}D_{22}$ at 10 °C, d = 78 Å. The Wigner–Seitz cell is drawn in to guide the eye. The small high spots of scattering density in the corner of the Wigner–Seitz cell along the [1,1] direction can be attributed to scattering from the deuterated decane. The unusual low density square regions are due to series termination effects in this low-resolution reconstruction.

determination of the decane distribution within the unit cell.

The phasing of the deuterated decane data was accomplished by observing how the peak amplitudes shift with added decane. At 25 °C, adding deuterated decane to the DOPE + H_2O sample changes the (1,1) peak amplitude from −3.15 to 0. Similarly, it takes the amplitude of the (1,1) in DOPE + D_2O from 0 to ±2.69. This can only occur if it adds in positively at that peak; therefore, the phase of the DOPE + H_2O + $C_{10}D_{22}$ (1,1) peak should be +. The other peak amplitudes also change smoothly with added decane but their signs do not change, so the resulting phasing is +,+,−,−. One should note that this analysis works equally well for any of the temperatures, since no phase change was observed with temperature. This is not surprising because the peak phases are expected to change slowly with temperature for H_{II} phase diffraction [see Turner and Gruner (1992)]. We also should note that this phase assignment agrees with model predictions of arbitrarily distributed deuterated decane within the hydrocarbon chains of the lipid.

Distribution of Decane. Figure 3 shows the reconstruction of DOPE + D_2O with the deuterated decane at 10 °C, assuming the +,+,−,− phasing. The obvious feature is the high scattering density in the region at the corner of the Wigner–Seitz cell along the [1,1] direction, i.e., in the interstitial region (see Figure 1a in the accompanying X-ray paper). These data show that decane does, in fact, partition preferentially into that region. A similar localization of the decane was observed for both the 25 and 50 °C data; however, it is not as pronounced as the temperature is increased. This is expected because the interstitial region occupies a smaller fraction of the total hydrocarbon volume as the water fraction decreases with increasing temperature. See Figure 19 of the preceding paper in this issue (Turner & Gruner, 1992) for a more complete description of this phenomena. For this reason, the following analysis concentrates on the most localized data, that at 10 °C.

The actual distribution of decane within the unit cell can be determined by subtracting the unit cell reconstruction of DOPE + D_2O + $C_{10}H_{22}$ from the reconstruction of DOPE + D_2O + $C_{10}D_{22}$. Since all of the diffraction amplitudes are already normalized to a relative scale, only the constant offset needs to be determined. This was done by making the D_2O regions in each reconstruction overlap as well as possible, so that the difference between the two reconstructions average to zero in that region. The regions will never subtract perfectly because of cutoff effects in the low-resolution Fourier series. This procedure relies on the assumption that very little of the decane has partitioned into the water (D_2O) region, which is justified by the very low solubility of decane in water. Figure 4a shows the difference map, indicating the distribution of decane in the unit cell as seen at this resolution. Figure 4b shows cross sections of the difference map along the [1,1] and [1,0] direction. The decane is confined to the edges of the Wigner–Seitz cell and is predominantly found along the [1,1] direction.

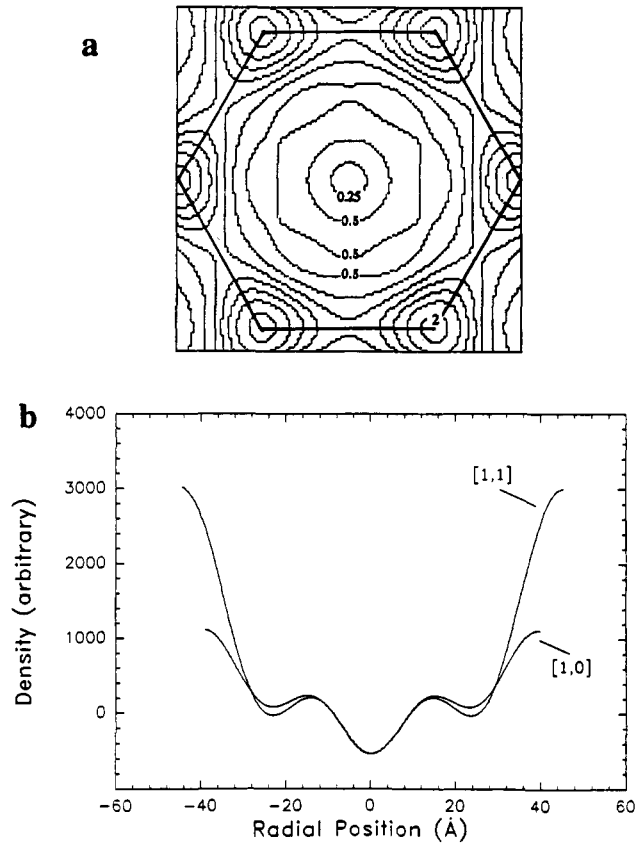

FIGURE 4: (a) Neutron scattering denstiy difference map at 10 °C, d = 78 Å. The data were derived by subtracting the DOPE + D_2O + $C_{10}H_{22}$ map from the DOPE + D_2O + $C_{10}D_{22}$ map. The strong peaks along the [1,1] direction are now very obvious, and this map can be thought of as a distribution map for deuterated decane within the Wigner–Seitz cell. The contour lines are on the same scale as the unsubtracted reconstructions. (b) Cross sections of the above map along the [1,0] and [1,1] directions. The scattering density at the end of the chains in the [1,1] direction is three times as strong as the scattering density in the [1,0] direction. This implies that most of the decane is partitioning along the [1,1] direction in the lattice.

The distribution can be quantified. Integrating the scattering density radially out from the center of the water core gives the angular distribution of decane within the unit cell. Properly normalized, this distribution is the fraction of decane by volume lying along a particular direction θ. Figure 5 shows the normalized distribution of decane as a function of angle at 10 °C; 0° corresponds to the [1,0] direction while 30° is along the [1,1] direction. For simplicity, the data are fit to a parabola, which is normalized such that the integral under the curve from 0 to 30° is unity when the angle is measured in radians. The parabola $F(\theta) = 0.989 - 0.1439\theta + 10.486\theta^2$

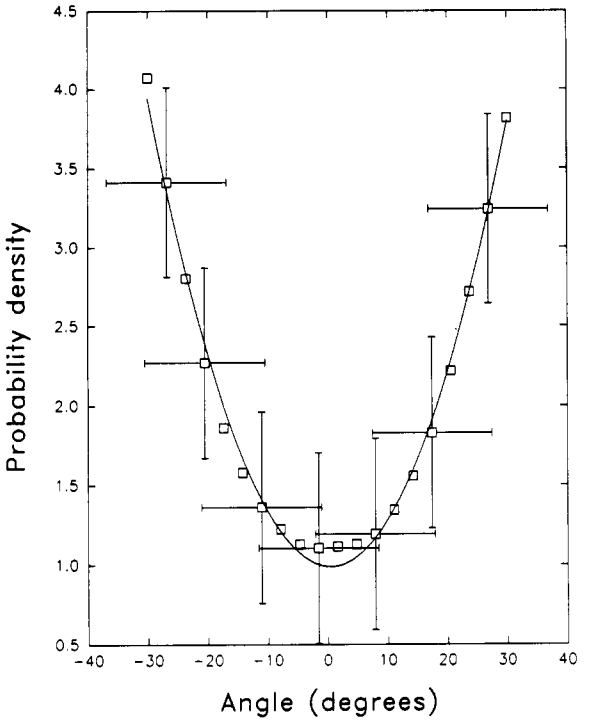

FIGURE 5: Normalized distribution of decane as a function of angle calculated at 10 °C. This has been determined by integrating pie-shaped strips from the center of the water core to the edge of the Wigner–Seitz cell for the decane distribution shown in Figure 6. The angle is measured with respect to the [1,0] direction, so that 30° points along the [1,1] direction. This curve was then fit to a quadratic (solid line; see text) and normalized such that the integral under the curve from 0 to 30° was 1 when the angle is measured in radians. The errors bars indicate the region within which the curve may slide and change its shape. The points will not show normal scatter within these error bars because the low-resolution Fourier reconstruction acts as a high-frequency filter, effectively smoothing the data so it will always be found on a smooth curve. This plot shows that the integrated decane along the [1,1] direction is roughly 3.5 times the integrated dodecane along the [1,0] direction.

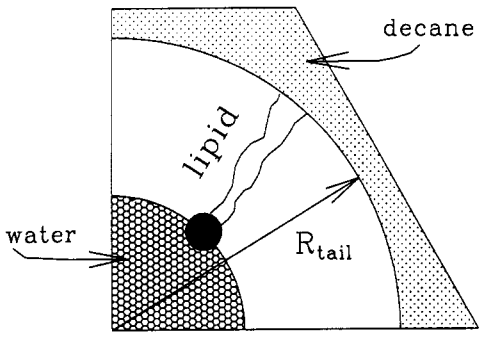

FIGURE 6: Definition of the lipid volume length (R_{tail}) with added decane. To obtain this length, we imagine that the decane partitions along the edge of the Wigner–Seitz cell distinctly from the lipid and water regions. Then the shape of the curve defining the inner edge of the decane region is determined by forcing its integrated distribution of decane (as a function of angle) to match the measured distribution in Figure 5.

gives the fit to the distribution with θ in radians. It should be noted that this is a resolution-limited distribution, and it is possible that the true distribution is even more strongly peaked toward the [1,1] direction.

Angular Distribution of Decane. The decane distribution function $F(\theta)$ may be used to define a volume distribution by imagining it to be confined to the perimeter of the hexagonal Wigner–Seitz cell, with all the lipid enclosed within this decane shell (Figure 6). This does not mean, of course, that the data imply that the decane and lipid chains occupy distinct volumes; rather, this should be considered to be a visualization device which conveys the axially asymmetric volume distribution of decane. More importantly, as shall be seen, the remaining volume of the Wigner–Seitz cell is more axially symmetric with, than without, the decane. This is significant because it is the axial asymmetry of the lipid chain conformations required to fill the Wigner–Seitz cell which is responsible for the angular distribution of the decane.

This procedure was applied to DOPE at 10 °C, which has $d = 78 \pm 0.5$ Å and $R_w = 22.8 \pm 0.5$ Å. Since the d-spacing of the decane sample is also 78 ± 1.5 Å, the radius of the water core can be estimated from the increased hydrocarbon volume (assuming bulk alkane density) to be 19.1 ± 3.0 Å, from which the water volume fraction can be estimated at 0.218. Given these values, the volume decane filling the region between 0 and 30° in the Wigner–Seitz cell is

$$V_{decane} = \frac{l}{12}\left[\frac{V_{decane}}{V_{lipid} + V_{decane}}\right]\left[\frac{V_{lipid} + V_{decane}}{V_{cell}}\right]A_{cell} \quad (3)$$

$$V_{decane} = \frac{l}{12}\left[(0.119)(0.782)\frac{\sqrt{3}}{2}(78\ \text{Å})^2\right] \quad (4)$$

$$V_{decane} = 40.86l\ \text{Å}^2 \quad (5)$$

where the subscripts specify the component volumes involved, A_{cell} is the cross-sectional area of the unit cell, and l is an arbitrary length of the hexagonal tube which will drop out of all further calculations.

To determine the angular variation in the lipid length, assume that the decane fills some shape near the edge of the unit cell whose radial integral at any angle is given by $F(\theta)$. The inner edge of this shape marks the assumed location of the end of the lipid chains. If $R(\theta)$ is the radius to the edge of the Wigner–Seitz cell and $R'(\theta)$ is the radius to the edge of the decane region, then we have (define $A_{decane} = V_{decane}/l$)

$$F(\theta)A_{decane}\delta\theta = \frac{\delta\theta}{2}[R^2(\theta) - R'^2(\theta)] \quad (6)$$

where the solution for $R'(\theta)$ is

$$R'(\theta) = \sqrt{[R^2(\theta) - 2F(\theta)A_{decane}]} \quad (7)$$

Figure 7a shows the plot of $R'(\theta)$ for DOPE + decane using $F(\theta)$ and A_{decane} from above. Given $R'(\theta)$, the angularly dependant lipid length $l(\theta)$ can be easily calculated as $l(\theta) = R'(\theta) = R_w$, as shown in Figure 7b. The greatest uncertainty in $l(\theta)$ comes from the estimated radius of the water core R_w and the large error in the estimate of d, so the whole curve may shift several angstroms with respect to the length without decane. It is immediately clear, however, that the distribution of lengths is much narrower with decane. In fact, the difference between d_{max} and $d_{H_{II}}$ is reduced by more than 2.5 Å when decane is added, approximately 15% of the total lipid length. The decane is allowing the lipid environment to be more uniform.

The uncertainty in the vertical displacement of the lipid length curves can largely be eliminated by using values for R_w and d taken from higher resolution X-ray diffraction data. If the alkane distribution within the unit cell is assumed to only weakly depend on the alkane chain length, then the DOPE + dodecane X-ray data can be used by assuming that dodecane distributes identically to decane at this resolution. Using data for a sample with 10% dodecane by weight at 10 °C, $R'(\theta)$ and $l(\theta)$ can be calculated as above [see the preceding paper in this issue, Turner and Gruner (1992), for these data]. The

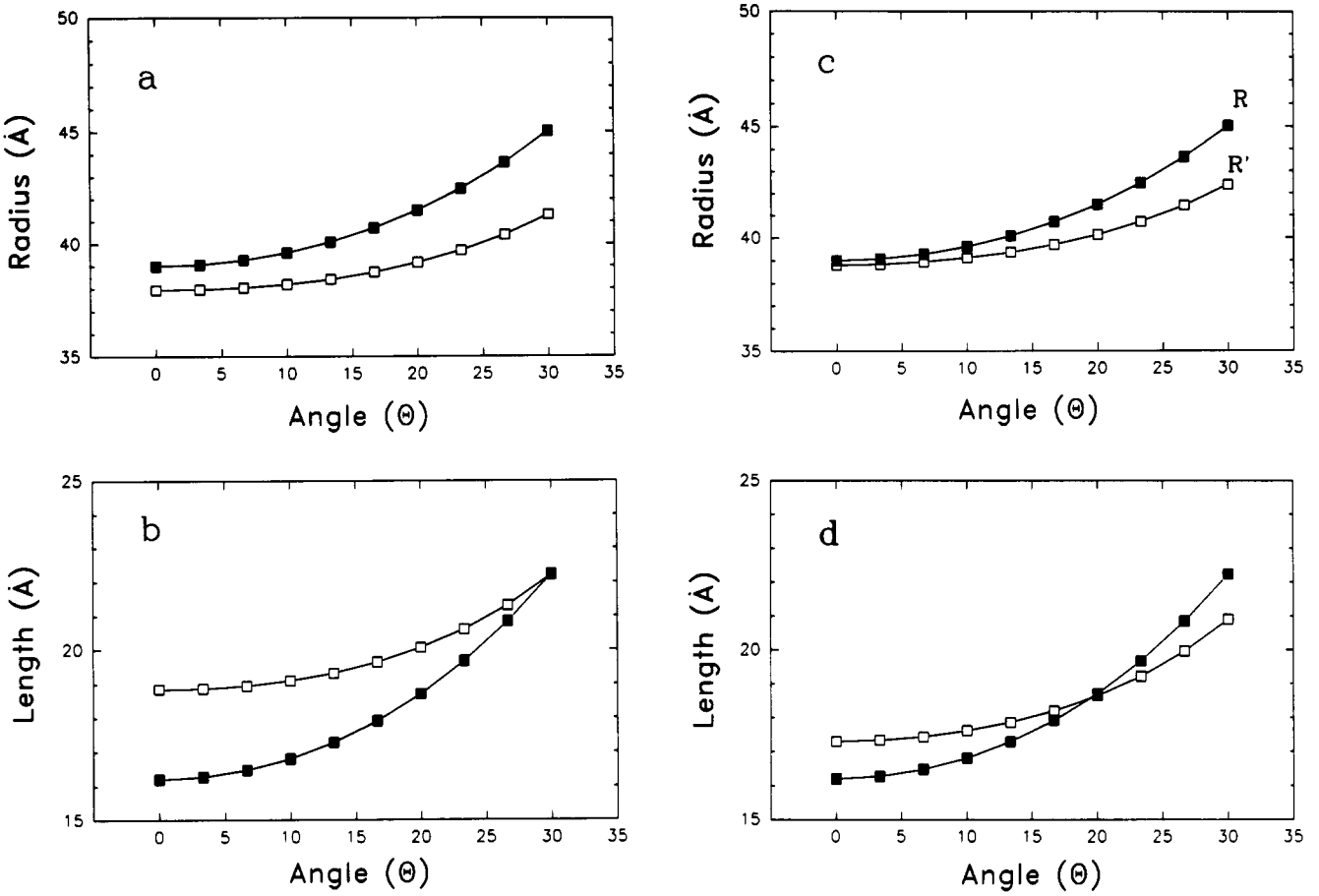

FIGURE 7: (a) Lipid volume length, R_{tail}, as a function of angle for DOPE + excess water (filled squares; this is the edge of the Wigner–Seitz cell) and DOPE + 9.5% decane + excess water (open squares) at 10 °C. R_{tail} was calculated as described in the legend to Figure 6, with the angle running from 0° = [1,0] direction to 30° = [1,1] direction. (b) Lipid length, calculated by subtracting the radius of the water core from the corresponding value of lipid volume length in panel a for the sample with (open squares) or without (filled squares) decane. The length at 0° is $d_{H_{II}}$ and the length at 30° is d_{max} for the sample without decane. The entire decane curve may shift up or down by 1.5–2 Å because the radius of the water core in the decane sample is only known to this precision. The point to notice, however, is that the added decane makes the width of the distribution of lipid lengths much narrower, thus making the lipid hydrocarbon environment more uniform than in the pure DOPE + excess water system. (c) R_{tail} for DOPE + excess water (filled squares) and DOPE + 10% dodecane + excess water (open squares) at 10 °C, assuming that dodecane distributes itself within the unit cell like decane. The dodecane data are taken from the accompanying paper on X-ray diffraction results on the H_{II} phase (Turner & Gruner, 1992). (d) Lipid length distribution calculated by subtracting the water core radius from the lipid tail location shown in panel a. The open squares denote the sample with dodecane, and the filled squares are without dodecane. In this case the radius of the water core in the 10% dodecane sample is known to ±0.5 Å, so the dodecane lipid length curve can only shift vertically by ±0.5 Å. This plot shows that the lipid in the pure DOPE phase is probably stretched along the [1,1] direction and compressed along the [1,0] direction. The dodecane reduces the magnitude of these variations.

curves are shown in Figure 7c,d. Since the radius of the water and d-spacing are known to ±0.5 Å, the $l(\theta)$ curve is restricted to move only ±0.5 Å relative to the curve without dodecane. The lipid thickness along the [1,1] direction, d_{max}, is reduced by 1.3 Å, while the thickness along the [1,0] direction, $d_{H_{II}}$, increases by roughly the same amount. Without dodecane the lipid is compressed along the [1,0] direction and stretched along the [1,1] direction with some of this stress released when alkane is added. It is interesting to note that the average length is about 18.5 Å with or without added alkane, nearly the same as the monolayer thickness in the lamellar phase (Gruner et al., 1988).

Discussion

Alkanes and polyisoprenes are potent promoters of H_{II} phases. Less than 5 dry wt % of dodecane can lower the L_α–H_{II} transition temperature, T_{bh}, of some systems by about 50 °C. Less than 5 dry wt % of a 1000 dalton molecular weight *cis*-polyisoprene lowers T_{bh} of POPE (1-palmitoyl-2-oleoylphosphatidylethanolamines) by over 20 °C (O. Narayan and S. M. Gruner, unpublished observations). What is the mechanism whereby these hydrophobes lower T_{bh}? According to the Kirk et al. (1984) model, the dominant feature controlling the L_α–H_{II} phase transition of electrically neutral lipid systems with excess water is a geometrically frustrated competition between free energies associated with a spontaneous curvature of the lipid monolayers and the axial asymmetries due to packing of the H_{II} tubes. The spontaneous curvature drives the tendency for the layers to curl, while the axial asymmetries mitigate against curvature. Accordingly, it is expected that molecules which are capable of reducing the axial asymmetries of the lipid chains in H_{II} phases would lower the energetic cost of H_{II} phase geometries and promote the formation of low-temperature H_{II} phases (Kirk & Gruner, 1985).

Axial asymmetries in the H_{II} phase are a consequence of the fact that the lipid chains must fill all of the hydrophobic volume of the H_{II} lattice. Entropic considerations demand that the chains perform this function by filling the hydrophobic volume as symmetrically as possible. As in any fluid polymeric system, regions large density fluctuations are particularly entropically expensive. In the preceding paper in this issue, a high-resolution X-ray diffraction analysis was performed and used to demonstrate that the mean local electron density of

the lipid hydrocarbon in the direction of the interstitial "triangle" (see Figure 4) varied greatly from the mean density of the chain region as a whole as the L_α–H_{II} phase transition temperature is approached from above [see Figure 19 of Turner and Gruner (1992)], indicative of the increasing energetic cost of maintaining an H_{II} geometry. While this observation alone strongly suggests the Kirk and Gruner (1984) mechanism of alkane action, it was desirable to obtain confirmation by direct structural means.

The high neutron scattering length density contrast of a perdeuterated alkane added to a protonated lipid system afforded a method of directly localizing an alkane within an H_{II} phase. The weakness of the diffraction and the consequent limitations of resolution of the neutron data complicated the solution of the structure and the localization of the alkane. By utilizing the information from the high-resolution X-ray structure (Turner & Gruner, 1992), however, the neutron data could be phased and the lattice reconstructed (Figures 2 and 3). Additional information was obtained by examining the difference structure of a DOPE–water system in the presence of protonated vs deuterated decane (Figure 4), where the only difference between the two structures results from the substitution of the decane protons by deuterons. The largest variations in the difference map (Figure 4a) are in the interstitial region, directly demonstrating that this is a primary site of the localization of the decane.

Even at the low resolution of the reconstruction, there is a distinct 6-fold periodic variation of probability of occurrence of the decane as a function of the angle around an H_{II} tube with respect to the lattice directions. The resolution-limited probability of occurrence of a decane deuteron as a function of angle was determined by radially integrating the effective deuteron density in narrow-angle pie-shaped wedges out to the edges of the Wigner–Seitz cell (Figure 5). A way of visualizing this probability distribution is to imagine that all the decane is pushed out against the walls of the hexagonal Wigner–Seitz cell, with the rest of the hydrophobic volume being occupied by the lipid chains (Figure 6). This defines a length of the remaining lipid volume (R_{tail} in Figure 6), which varies with the angle around the H_{II} tube. In the absence of alkane, this length simply traces out the Wigner–Seitz cell; the large variation in the [1,0] relative to the [1,1] direction is simply the axial asymmetry dictated by the H_{II} lattice. In the presence of dodecane, however, the variation in this length is reduced, indicative of the reduced axial asymmetry (Figure 7). While this visualization should not be taken too literally, since the lipid chains and the decane are not expected to aggregate into distinct volumes, it is of interest that the mean length of the lipid chain volume is about the same as the monolayer thickness of the L_α phase of DOPE.

The use of neutron diffraction opens exciting possibilities of probing the free energy of packing hydrocarbon chains in the H_{II} lattice. In the curvature vs hydrocarbon packing model (Kirk et al., 1984), the free energies of bending the lipid monolayer and of packing the hydrocarbon chains in the H_{II} phase are only weakly coupled and may be considered as distinct free energies. An osmotic method for measuring the bending energy has been devised (Gruner et al., 1986; Rand et al., 1990), but there still is no known method for probing the free energy of packing the lipid chains. A quantitative approach is offered by the alkane distribution function in that the one expects the alkane distribution to be governed by a Boltzmann distribution, i.e., the probability of occurrence in one part of the lattice with respect to another should be governed by the difference in the free energies of partitioning the alkane between the two parts of the lattice. Another exciting possibility along these lines is to specifically deuterate the terminal methyls of the lipid chains and determine the distribution of the ends of the chains. This would not only help in determining the free energy of the moving chain ends about the lattice but would also be a powerful constraint on statistical mechanical models of the lipid chains [e.g., Ben-Shaul et al. (1984, 1985)].

In conclusion, a combined X-ray and neutron diffraction analysis proves that decane distributes in an axially asymmetric fashion in the DOPE H_{II} phase. Since the H_{II}-promoting effect of decane is also observed with different hydrophobes and with different lipid systems, it appears likely that the hydrophobe distribution in these systems will also be axially asymmetric.

Acknowledgments

We thank William Dozier for assistance with the collection of the neutron diffraction data. D.C.T. thanks Dr. Mark Tate, Dr. E. Shyamsunder, and Onuttom Narayan for useful discussions. We gratefully acknowledge the Brookhaven National Laboratory for granting beam time on the H9 small-angle spectrometer and the expertise provided by D. Schneider.

Registry No. DOPE, 2462-63-7; *n*-decane, 124-18-5.

References

Ben-Shaul, A., Szleifer, I., & Gelbart, W. M. (1984) *Proc. Natl. Acad. Sci. U.S.A. 81*, 4601–4605.

Ben-Shaul, A., Szleifer, I., & Gelbart, W. M. (1985) *J. Chem. Phys. 83*, 3597–3611.

Büldt, G., Gally, H., Seelig, J., & Zaccai, G. (1979) *J. Mol. Biol. 134*, 673–691.

Cabane, B. (1986) in *Surfactant Solutions: New Methods of* Investigation (Zana, R., Ed.) Vol. 22, Marcel Dekker, New York.

Cullis, P. R., Hope, M. J., de Kruijff, B., Verkleij, A. J., & Tilcock, C. P. S. (1985) in *Phospholipids and Cellular Regulations* (Kou, J. F., Ed.) Vol. I, pp 1–59, CRC Press, Boca Raton, FL.

Dean, J. A., Ed. (1985) *Lange's Handbook of Chemistry*, McGraw Hill, New York.

Gruner, S. M. (1985) *Proc. Natl. Acad. Sci. U.S.A. 82*, 3665–3669.

Gruner, S. M., Parsegian, V. A., & Rand, R. P. (1986) *Faraday Discuss. Chem. Soc. 81*, 29–37.

Gruner, S. M., Tate, M. W., Kirk, G. L., So, P. T. C., Turner, D. C., Keane, D. T., Tilcock, C. P. S., & Cullis, P. R. (1988) *Biochemistry 27*, 2853–2866.

HFBR Handbook (1983) Brookhaven National Lab Informal Report 24182.

Jacobs, R. E., & White, S. H. (1989) *Biochemistry 28*, 3421–3437.

Kirk, G. L., & Gruner, S. M. (1985) *J. Phys. (Paris) 46*, 761–769.

Kirk, G. L., Gruner, S. M., & Stein, D. E. (1984) *Biochemistry, 23*, 1092–1102.

Knott, R. B., & Schoenborn, B. P. (1986) *Methods Enzymol. 127*, 217–229.

Rand, R. P., Fuller, N. L., Gruner, S. M., & Parsegian, V. A. (1990) *Biochemistry 29*, 76–87.

Siegel, D., Banschbach, J., & Yeagle, P. L. (1989) *Biochemistry 28*, 5010–5019.

Sjölund, M., Lindblom, G., Rilfors, L., & Arvidson, G. (1987) *Biophys. J. 52*, 145–153.

Sjölund, M., Rilfors, L., & Lindblom, G. (1989) *Biochemistry 28*, 1323–1329.

Turner, D. C. (1990) Ph.D. Dissertation, Princeton University, Princeton, NJ.
Turner, D. C., & Gruner, S. M. (1992) *Biochemistry* (preceding paper in this issue).
Warren, B. E. (1969) *X-ray Diffraction*, Addison-Wesley, Reading, MA.
Weiner, M. C., Suter, R. M., & Nagle, J. F. (1989) *Biophys. J. 55*, 315–325.
White, S. H., King, G. I., & Cain, J. E. (1981) *Nature 290*, 161–163.
Worcester, D. L., & Franks, N. P. (1976) *J. Mol. Biol. 100*, 359–378.

Binding of Verocytotoxin 1 to Its Receptor Is Influenced by Differences in Receptor Fatty Acid Content†

A. Pellizzari,‡,§ H. Pang,‖ and C. A. Lingwood*,‡,§,⊥,#

Department of Microbiology, The Hospital for Sick Children, 555 University Avenue, Toronto, Ontario M5G 1X8, Canada, Departments of Microbiology, Medical Genetics, and Biochemistry, University of Toronto, Toronto, Ontario M5S 1A8, Canada, and Department of Clinical Biochemistry, University of Toronto, Toronto, Ontario M5G 1L5, Canada

Received December 28, 1990; Revised Manuscript Received October 16, 1991

ABSTRACT: Globotriaosylceramide [(Galα1–4Galβ1–4Glc-ceramide (Gb_3)] was separated from human kidney, and the fatty acid composition was determined. Semisynthetic Gb_3 molecular species of corresponding fatty acid chain length were prepared and compared for verotoxin (VT) binding affinity by TLC overlay, and a quantitative binding assay was performed in the presence of auxiliary lipids. Our results indicate that, within the natural range, fatty acid chain length has little effect on verotoxin binding but that Gb_3 molecular species containing different fatty acids can interact to provide a higher affinity toxin receptor than any of the individual component receptor species. Receptor function as assayed by TLC overlay was not always found to correlate with binding in a lipid environment. Short-chain fatty acid Gb_3 molecular species could not function as VT receptors under these conditions. Evidence is presented to suggest that fatty acid chain length can have a stereoselective effect on carbohydrate conformation.

Strains of *Escherichia coli* (verotoxin-producing *E. coli*, VTEC) produce at least two immunologically distinct verocytotoxins (VT1 and VT2) that have been associated with hemorrhagic colitis (Pai et al., 1984) and the hemolytic uremic syndrome (HUS) (Karmali et al., 1985). HUS is characterized by microangiopathic hemolytic anemia and thrombocytopenia and is the leading cause of acute renal failure of children in developed countries (Karmali, 1989).

Verocytotoxins are subunit toxins made up of an active (A) subunit (MW 32 kDa) and as many as five binding (B) subunits (MW 7.7 kDa). Lingwood et al. (1987) have shown that VT1 binds specifically to glycosphingolipids such as globotriaosylceramide (Gb_3) and galabiosylceramide having a terminal Galα1–4Gal disaccharide sequence. The same glycolipid receptor has been found for VT2 (Waddell et al., 1988) and for Shiga toxin (Jacewicz et al., 1986; Lindberg et al., 1987). Gb_3 is the functional receptor for VT1 since a VT-resistant mutant Daudi cell line (Cohen et al., 1987) and a vero cell mutant (Pudymaitis et al., 1991) were found to lack Gb_3. Incorporation of Gb_3 into receptor-deficient Daudi cells resulted in the induction of VT sensitivity (Waddell et al., 1990).

Internalization of cell-bound VT1 is thought to occur by receptor-mediated endocytosis. Inside the cell the A subunit of VT1 is proteolytically nicked and reduced to the A1 fragment suppressing protein synthesis through the inhibition of elongation factor 1 dependent aminoacyl-tRNA binding to the 60S ribosome (Igarashi et al., 1987). However, the affinity of Gb_3 binding also defines cytotoxic potential of the holotoxin (Head et al., 1991).

Glycosphingolipids are components of the outer leaflet of the plasma membrane. They are thought to have roles in cell–cell interaction (Hakomori, 1981), as cell-surface receptors for some pathogenic bacteria (Stromberg et al., 1988), and function as antigens through their sugars (Marcus et al., 1981). Most attention has focused on the carbohydrate moiety of the glycolipids while the ceramide has been thought to act simply as an anchor in the plasma membrane. Studies by Kannagi et al. (1982) have shown that changes in the ceramide composition of the glycolipids were associated with variations in the reactivity of different cells with glycolipid-specific antibody. Changes in the surface exposure of sulfatide for antibody have also been shown to follow ceramide modification (Crook et al., 1986). Furthermore, the ceramide moiety of Gb_3 has been implicated in the binding of verotoxins to Gb_3 since digalactosyldiglyceride, containing the same terminal Galα1–4Gal sequence as Gb_3 and galabiosylceramide but linked to a glycerol moiety, showed no VT-binding activity (Lingwood et al., 1987; Waddell et al., 1988). Thus, the lipid portion of the molecule may affect the reactivity of glycolipids with various ligands by influencing the availability of the hydrophilic carbohydrate moiety.

Studies by Boyd and Lingwood (1989) have shown Gb_3 to be a major component of the human renal glycolipid fraction. However, changes in Gb_3 concentration could not explain the age-related incidence of HUS. If the lipid moiety were to influence binding, changes in the ceramide composition of Gb_3 might define VTEC-induced pathogenesis. The human renal

† This study was supported by Medical Research Council of Canada Grant MT 6499 and program Grant PG 11123. A.P. was the recipient of an Ontario Graduate Scholarship.

* Corresponding author.
‡ Department of Microbiology, The Hospital for Sick Children.
§ Department of Microbiology, University of Toronto.
‖ Department of Medical Genetics, University of Toronto.
⊥ Department of Clinical Biochemistry, University of Toronto.
Department of Biochemistry, University of Toronto.

0006-2960/92/0431-1363$03.00/0